Annals of Biomedical Engineering, Vol. 51, No. 1, January 2023 *(© 2022)* pp. 189–199
https://doi.org/10.1007/s10439-022-03075-z

S.I. : Modeling for Advancing Regulatory Science

Semi-Automated Construction of Patient-Specific Aortic Valves from Computed Tomography Images

DAN LIOR,[1] CHARLES PUELZ,[1] COLIN EDWARDS,[2] SILVANA MOLOSSI,[1] BOYCE E. GRIFFITH,[3,4] RAVI K. BIRLA,[5] and CRAIG G. RUSIN[1]

[1]Division of Cardiology, Department of Pediatrics, Baylor College of Medicine and Texas Children's Hospital, Houston, TX, USA; [2]Department of Mechanical Engineering, Rice University, Houston, TX, USA; [3]Departments of Mathematics, Biomedical Engineering, and Applied Physical Sciences, and Carolina Center for Interdisciplinary Applied Mathematics, University of North Carolina, Chapel Hill, NC, USA; [4]Computational Medicine Program and McAllister Heart Institute, University of North Carolina School of Medicine, Chapel Hill, NC, USA; and [5]Division of Congenital Heart Surgery, Department of Pediatric Surgery, Baylor College of Medicine and Texas Children's Hospital, Houston, TX, USA

(Received 15 April 2022; accepted 4 September 2022; published online 8 October 2022)

Associate Editor Joel Stitzel oversaw the review of this article.

Abstract—This paper presents a semi-automatic method for the construction of volumetric models of the aortic valve using computed tomography angiography images. Although the aortic valve typically cannot be segmented directly from a computed tomography angiography image, the method described herein uses manually selected samples of an aortic segmentation derived from this image to inform the construction. These samples capture certain physiologic landmarks and are used to construct a volumetric valve model. As a demonstration of the capabilities of this method, valve models for 25 pediatric patients are created. A selected valve anatomy is used to perform fluid–structure interaction simulations using the immersed finite element/difference method with physiologic driving and loading conditions. Simulation results demonstrate this method creates a functional valve that opens and closes normally and generates pressure and flow waveforms that are similar to those observed clinically.

Keywords—Aortic valve, Anatomical reconstruction, Fluid–structure interaction, Computed tomography, Immersed finite element/difference method.

INTRODUCTION

In a healthy human heart, the aortic valve contains three leaflets and separates the left ventricle from the systemic arterial tree. The valve allows for high pressure and velocity flow from the left ventricle to pass through the aorta and eventually to perfuse the systemic organs.[23,30] A healthy aortic valve closes and sustains a large pressure gradient when the left ventricle is relaxed.[3,23] These extreme operating conditions amplify possible clinical issues with this valve, such as aortic stenosis or bicuspid valve disease.[1,29] Due to its importance in the physiology of a healthy circulation, substantial experimental, clinical, and computational research has been devoted to understanding aortic valve function.[2,4,9,22]

Previous work has focused on the characterization and parametrization of human valve anatomies, often for their use in computational models. Valve anatomies and corresponding models for immersed boundary fluid-structure interaction (FSI) simulations have been created using a "design-based" approach. Variations of this approach generate leaflet geometries by solving partial differential equations for the mechanical equilibrium of the leaflets under physiologic loading conditions. For example, Peskin and McQueen formulated equilibrium equations for the aortic valve and computed fractal-like structures for each of the leaflets.[26] More recently, Kaiser *et al.* devised similar models for the aortic valve and used the resulting model in immersed boundary simulations.[16] Other approaches include the creation of aortic valve geometries from echocardiographic or computed tomographic data. Rego *et al.* created leaflet segmentations from real-time 3D echocardiagraphic

Address correspondence to Charles Puelz, Division of Cardiology, Department of Pediatrics, Baylor College of Medicine and Texas Children's Hospital, Houston, TX, USA. Electronic mail: charles.puelz@bcm.edu

Dan Lior and Charles Puelz are co-first authors.

data in order to non-invasively calculate leaflet strains.[27] Haj-Ali *et al.* developed a parametrization of the combined aortic sinus and valve geometry and tested their approach using 3D transesophageal electrocardiogram (ECG) data.[11] Morganti *et al.* created a patient-specific non-uniform rational B-Spline (NURBS) representation of aortic leaflet and aortic root surfaces from computed tomography (CT) images.[22] These NURBS surfaces were then used in finite element simulations of aortic valve closure. Chen *et al.* devised a method for reconstructing *in vivo* anatomies for a prosthetic aortic valve and stent using CT data.[7] Lastly, Liang *et al.* used CT data to implement a machine learning framework for aortic valve reconstruction.[19]

Related work has focused on geometric construction of the mitral and tricuspid valves. Kaiser *et al.* constructed a mitral valve geometry with a design-based approach and performed numerical simulations using the immersed boundary method.[15] Khalighi *et al.* described an approach for precise geometric modeling of the mitral valve using micro-CT data.[17] In their work, they implemented a super-quadratic parametrization of the mitral leaflets. Mathur *et al.* constructed a geometric model of the tricuspid valve by parametrizing the free-edge height along the curved determined by the valve annulus.[20] Johnson *et al.* described a template-based approach for geometric modeling and simulation of the tricuspid valve that is independent of imaging modality.[14]

The focus of this work is the semi-automatic construction of geometric models of the aortic valve for use in simulating blood flow through the pediatric aorta and valve leaflets. The aortic vessel anatomy is readily acquired from computed tomography angiography (CTA) data, but the resolution of clinically acquired CTA images is typically too coarse for reconstructing the leaflet anatomy. This paper describes a process for generating patient-specific anatomical models of the aortic valve using the aortic vessel segmentation and a manually selected sample from this segmentation that approximates certain physiologic landmarks called the interleaflet triangles.[31] Leaflet anatomies are constructed in the closed configuration through a simple and interpretable constrained optimization problem. This procedure allows for the fitting of parametrized leaflet geometries within the asymmetric aortic sinuses, the incorporation of variable leaflet thickness, and the inclusion of the valve center position, if visible in the CTA image.

METHODS

CTA images from a cohort of 25 pediatric patients are used to construct volumetric valve models as detailed in "Construction of the Volumetric Valve Model" section. Additionally, for a representative patient in the cohort, an FSI simulation is performed. To facilitate the simulation, the volumetric valve model for this patient is first extended to a *valve assembly model* that includes a labeled tetrahedral mesh of the valve and the surrounding aorta. The construction of the valve assembly model is described in "Construction of the Valve Assembly Model" section and the FSI simulation in "Simulation of Flow Through the Constructed Valve Model" section.

Construction of the Volumetric Valve Model

Segmentation and Processing of the Aorta from CTA Data

The valve model construction begins with a CTA image containing a section of the aorta properly including the sinuses. The study protocol for collecting this data was approved by the Baylor College of Medicine Institutional Review Board (H-32955, last approved on August 16, 2021). All studies were performed on a 320-detector scanner (Aquilion ONE; Toshiba Medical Systems, Japan) and dual-source CT scanner (Somatom Force; Siemens Healthineers, Erlangen, Germany), without sedation, during volitional breath-holding. Images were obtained using retrospective ECG gating. A triangulated surface representation of the aortic lumen is segmented from the CTA image using 3D Slicer[1] and then processed using Meshmixer.[2] Refer to the left and middle panel of Fig. 1, respectively. The processing of the segmented surface consists of cropping, smoothing, remeshing and removing segmentation artifacts.

Selection of Sinus Samples

The processed aortic surface is used to identify the boundary between the aortic lumen and the lower half of the aortic sinuses (see the right panel of Fig. 1 and the first column of Fig. 2). Thin strips on the surface mesh that approximate this boundary, called the *sinus samples*, are manually selected in Meshmixer. Taken together, the sinus samples form a single continuous curve with three upward-facing cusps. These cusps are called the *interleaflet triangles* by Sutton *et al.*[31]

[1]3D Slicer is open-source software capable of image segmentation (https://www.slicer.org/).

[2]Meshmixer is a free software tool capable of manipulating stereolithography (STL) meshes (https://www.meshmixer.com/).

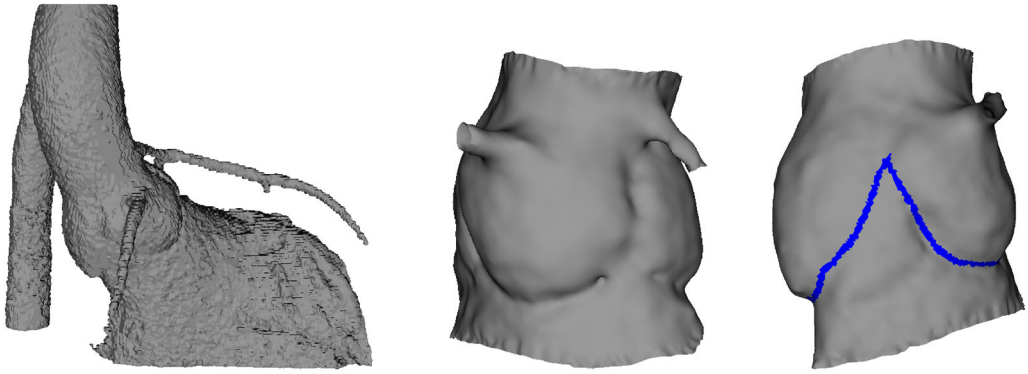

FIGURE 1. Triangulated surface segmented from a computed tomography angiography (CTA) image (left), the processed surface (middle), and the sinus samples (right).

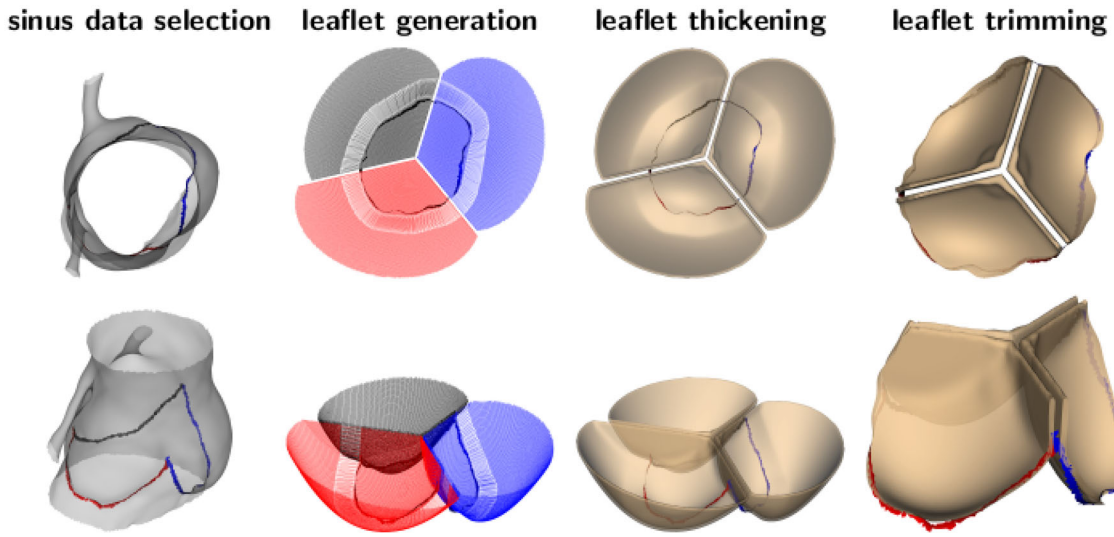

FIGURE 2. Aortic leaflet generation. The first column depicts the processed aortic segmentation. The second column depicts the raw leaflet surfaces. The third column depicts the thickened leaflet surfaces. The fourth column depicts the valve model trimmed along the segmented aortic lumen. The sinus samples appear in all the columns.

Generation of Lower Leaflet Surfaces

This section describes the generation of the lower (i.e., ventricle-facing) surfaces of the valve leaflets. The sinus samples associated with the three sinus boundaries are spatial regions denoted $\{\boldsymbol{x}_i^{(1)}\}$, $\{\boldsymbol{x}_i^{(2)}\}$, and $\{\boldsymbol{x}_i^{(3)}\}$. The centroids of these sets are $\boldsymbol{c}_1$, $\boldsymbol{c}_2$, and $\boldsymbol{c}_3$. By rotating the reference frame appropriately, $\boldsymbol{c}_1$, $\boldsymbol{c}_2$, and $\boldsymbol{c}_3$ can be assumed to lie on a horizontal plane. The *valve center*, $\boldsymbol{p}_{\text{center}}$, is:

$$\boldsymbol{p}_{\text{center}} = (\boldsymbol{c}_1 + \boldsymbol{c}_2 + \boldsymbol{c}_3)/3. \tag{1}$$

The *valve axis* is defined as the vertical line passing through $\boldsymbol{p}_{\text{center}}$.

Points $\boldsymbol{s}_{12}$, $\boldsymbol{s}_{13}$, and $\boldsymbol{s}_{23}$ approximate the positions of the cusps in the sinus data. As described above, these are the top vertices of the interleaflet triangles. More precisely, the point $\boldsymbol{s}_{12}$ is computed as:

$$(\tilde{\boldsymbol{x}}^{(1)}, \tilde{\boldsymbol{x}}^{(2)}) = \underset{ij}{\operatorname{argmin}} \|\boldsymbol{x}_i^{(1)} - \boldsymbol{x}_j^{(2)}\|, \tag{2}$$

$$\boldsymbol{s}_{12} = \frac{1}{2}\left(\tilde{\boldsymbol{x}}^{(1)} + \tilde{\boldsymbol{x}}^{(2)}\right). \tag{3}$$

The points $\boldsymbol{s}_{13}$ and $\boldsymbol{s}_{23}$ are computed in a similar manner. These points, shown in Fig. 3, are used to define the free edges of the leaflets.

The *valve apex* is the point $\boldsymbol{p}_{\text{apex}}$ where the valve leaflets meet. Since the valve apex is not discernable in the CTA images used in this study, it is assumed to lie on the valve axis at a distance h_{valve} above the valve center:

$$\boldsymbol{p}_{\text{apex}} = \boldsymbol{p}_{\text{center}} + h_{\text{valve}}\,\hat{\boldsymbol{k}}, \tag{4}$$

$$h_{\text{valve}} = 0.5 + \max\{\boldsymbol{s}_{12}\cdot\hat{\boldsymbol{k}}, \boldsymbol{s}_{23}\cdot\hat{\boldsymbol{k}}, \boldsymbol{s}_{13}\cdot\hat{\boldsymbol{k}}\}, \tag{5}$$

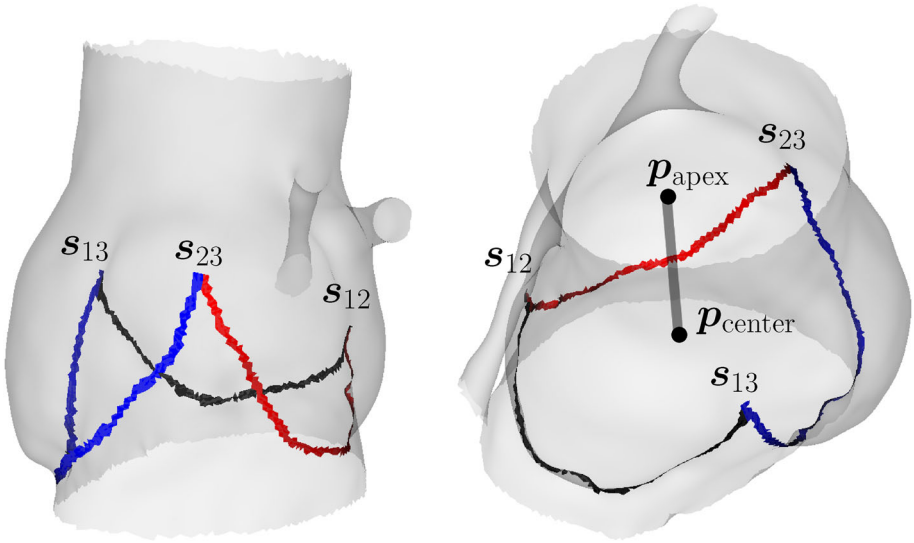

FIGURE 3. The points p_{center} and p_{apex} are the valve centroid and apex respectively. The points s_{12}, s_{23}, and s_{13} lie on planes through the free edges of the leaflets.

where $\hat{\boldsymbol{k}}$ is the unit vector along the positive z axis. The free edge between leaflets 1 and 2 corresponds to the plane containing the points $\{\boldsymbol{s}_{12}, \boldsymbol{p}_{\text{center}}, \boldsymbol{p}_{\text{apex}}\}$.

Each leaflet surface is computed by fitting a certain quadric surface to the selected sinus samples together with two of the $\boldsymbol{s}_{ij}$'s defined above. For example, the quadric surface defining leaflet 2 is required to contain the points $\{\boldsymbol{s}_{12}, \boldsymbol{s}_{23}, \boldsymbol{p}_{\text{apex}}\}$. Quadric surfaces used in this paper are parameterized as:

$$z = f(x, y; a_{xx}, a_{yy}, a_{xy}, \hat{x}, \hat{y}, \hat{z}) := a_{xx}(x - \hat{x})^2 + a_{yy}(y - \hat{y})^2 + a_{xy}(x - \hat{x})(y - \hat{y}) + \hat{z}. \tag{6}$$

The notation (x, y, z) denotes a point in three-dimensional space, and $a_{xx}, a_{yy}, a_{xy}, \hat{x}, \hat{y}$, and $\hat{z}$ are the unknown parameters of the quadric surface. Define:

$$\boldsymbol{x} = (x, y, z), \tag{7}$$

$$\boldsymbol{\beta} = (a_{xx}, a_{yy}, a_{xy}, \hat{x}, \hat{y}, \hat{z}), \tag{8}$$

$$g(\boldsymbol{x}; \boldsymbol{\beta}) = z - f(x, y; a_{xx}, a_{yy}, a_{xy}, \hat{x}, \hat{y}, \hat{z}). \tag{9}$$

The objection function for each leaflet is:

$$J(a_{xx}, a_{yy}, a_{xy}, \hat{x}, \hat{y}, \hat{z}) = \frac{1}{N}\sum_{i=1}^{N} w_i \, | \, g(\boldsymbol{x}_i; a_{xx}, a_{yy}, a_{xy}, \hat{x}, \hat{y}, \hat{z}) \, |^2 + \frac{\lambda}{a_{xx} + a_{yy}}, \tag{10}$$

in which N denotes the number of points in the sinus sample. The second term above, controlled by the parameter $\lambda \geq 0$, penalizes small curvatures, thus avoiding flat surfaces. The *curvature weights* w_i are discussed in the Supplementary Material. The final constrained optimization problem for leaflet 2 is:

$$\underset{\boldsymbol{\beta}}{\text{minimize}} \; J(\boldsymbol{\beta}) \tag{11}$$

$$\text{subject to} \quad g(\boldsymbol{s}_{12}; \boldsymbol{\beta}) = g(\boldsymbol{s}_{23}; \boldsymbol{\beta}) = g(\boldsymbol{p}_{\text{apex}}; \boldsymbol{\beta}) = 0 \tag{12}$$

$$4\, a_{xx}\, a_{yy} - a_{xy}^2 \geq 0, \quad a_{xx} + a_{yy} \geq 0 \tag{13}$$

$$\hat{z} \geq z_{\text{min}}^{(2)} \tag{14}$$

Constraint (12) ensures the points $\boldsymbol{s}_{12}$, $\boldsymbol{s}_{23}$, and $\boldsymbol{p}_{\text{apex}}$ lie on the quadric surface. Constraint (13) expresses the positive semidefiniteness of the Hessian of the quadric surface. This ensures that the quadric surface is an upward opening paraboloid (as opposed to a different type of quadric surface, e.g. a hyperboloid). Let $z_{\text{min}}^{(1)}$, $z_{\text{min}}^{(2)}$, and $z_{\text{min}}^{(3)}$ be the minimum z values of the sinus samples. The last constraint, Eq. (14), avoids paraboloids whose vertices lie lower than the sinus data. The optimization problems for the other leaflets differ only in the sinus data, the objective function weights, and in Eqs. (12) and (14).

The process described above is implemented in MATLAB (The MathWorks, Natick, MA), and the optimization problem is solved using the `fmincon` function. Since the objective function potentially has multiple local minima, several candidate solutions are computed by varying the curvature penalization

parameter λ, the initial values for a_{xy}, and the curvature weights w_i.

The parameter λ takes the following values: $\{10^{-1}, 10^{-2}, 10^{-3}, 10^{-4}, 0\}$. The initial guess for a_{xy} takes the following values: $\{-10^{-1}, -10^{-2}, 0, 10^{-2}, 10^{-1}\}$. Initial guesses for a_{xx} and a_{yy} are 10^{-2}, and the initial guess for the paraboloid vertex $(\hat{x}, \hat{y}, \hat{z})$ is $\boldsymbol{p}_{\text{center}}$. Ranges of values for the curvature penalization parameter and initial guesses are determined empirically from tests on several patient data sets. For a fixed choice of the curvature weights w_i, curvature penalization parameter λ, and initial guess for a_{xy}, the paraboloid error is computed as the mean squared distance of the sinus data points to the computed paraboloid. The final optimal paraboloid minimizes this error.

The resulting paraboloids are automatically trimmed and projected to define the free edges of the leaflets. This process is described below for leaflet 2. Two planes, $\mathcal{P}_{\text{left}}$ and $\mathcal{P}_{\text{right}}$, are defined that specify the leaflet free edges on the left and right sides of the leaflet. For leaflet 2, the planes $\mathcal{P}_{\text{left}}$ and $\mathcal{P}_{\text{right}}$ are determined by the points $\{\boldsymbol{s}_{12}, \boldsymbol{p}_{\text{center}}, \boldsymbol{p}_{\text{apex}}\}$ and $\{\boldsymbol{s}_{23}, \boldsymbol{p}_{\text{center}}, \boldsymbol{p}_{\text{apex}}\}$, respectively. A third plane, $\mathcal{P}_{\text{middle}}$, is also defined by the points $\{\boldsymbol{c}_2, \boldsymbol{p}_{\text{center}}, \boldsymbol{p}_{\text{apex}}\}$ to separate the paraboloid into two parts. In order to trim and project the surfaces, the paraboloids are represented as sufficiently fine point clouds. Points to the left of $\mathcal{P}_{\text{middle}}$ and $\mathcal{P}_{\text{left}}$ are projected orthogonally onto $\mathcal{P}_{\text{left}}$, and points to the right of $\mathcal{P}_{\text{middle}}$ and $\mathcal{P}_{\text{right}}$ are projected orthogonally onto $\mathcal{P}_{\text{right}}$. The top of the paraboloids are trimmed by excluding points 1 mm higher than the z component of $\boldsymbol{p}_{\text{apex}}$. Because the paraboloid leaflets meet at $\boldsymbol{p}_{\text{apex}}$ only up to a certain tolerance (determined by the numerical optimization) and are represented as discrete point clouds, the 1 mm "buffer" is only a practical construct to ensure the resulting trimmed leaflets are sealed in the center. Triangulated surfaces for the bottom of the leaflets are constructed from the trimmed and projected point clouds.

The result of this process is displayed in the second column of Fig. 2. The sinus data are shown together with the trimmed and projected paraboloid surfaces. A small strip of elongated triangles can be seen close to the sinus data. This strip is created by translating part of the paraboloid surface radially outward in order to ensure proper penetration of the leaflet with the aortic lumen. The strip has no effect on the generated leaflet geometry; it is merely a temporary construction that aids in a trimming step required in the construction of the valve assembly model.

Thickening of Leaflet Surfaces to Create the Volumetric Valve Model

This section describes the construction of the upper (i.e., aorta-facing) leaflet surfaces. The upper and lower leaflet surfaces are then combined and trimmed to form the volumetric valve model. The thickness of the valve leaflets is assumed to be symmetric about the valve axis. Under this assumption, the upper surface of each leaflet is completely determined by its lower surface and a *radius profile* that specifies the thickness of a leaflet at any given (orthogonal) distance from the valve axis. A MATLAB script generates three upper surface meshes, given their corresponding lower surface meshes and a radius profile.

The prescribed radius profile $t(r)$ used to construct the valves here is motivated by the experimental data described in Sahasakul *et al.*[28] It is governed by two parameters: a thickness $t_{\max}$ for small radii (i.e., $t_{\max}$ is the thickness specified for the nodules of Arantius) and a thickness $t_{\min}$ for large radii (nearer to the aortic wall). As specified in Sahasakul *et al.*,[28] $t_{\min} = 0.4$ mm and $t_{\max} = 0.7$ mm.

A continuous transition from the maximum to the minimum thickness along the leaflet is achieved with a circular arc. The resulting thickness profile is defined as:

$$t(r) = \begin{cases} t_{\max}, & r \le r_{\text{small}}, \\ \sqrt{t_{\max}^2 - (r - r_{\text{small}})^2}, & r_{\text{small}} < r < r_{\text{large}}, \\ t_{\min}, & r \ge r_{\text{large}}. \end{cases} \tag{15}$$

Here, r_{small} is a parameter of the model that is governed by valve separation (a feature needed for the numerical simulations). More specifically, r_{small} is chosen to be approximately 1–2 times the finest Cartesian cell size based on prior experience in constructing valve models and also related to the discretization methods used by the immersed finite element/difference method.[12,18] If this parameter is too small, the valve leaflets will stick together, and if it is too large, there will be leakage through the valve when the leaflets are closed. The parameter r_{large} is given by:

$$r_{\text{large}} = r_{\text{small}} + \sqrt{t_{\max}^2 - t_{\min}^2}, \tag{16}$$

to ensure continuity of $t(r)$.

The thickened leaflet surfaces resulting from this process are shown in the third column of Fig. 2. The trimmed version of these leaflets, created from a Boolean operation between the aortic lumen and the thickened paraboloids, is shown in the fourth column of Fig. 2.

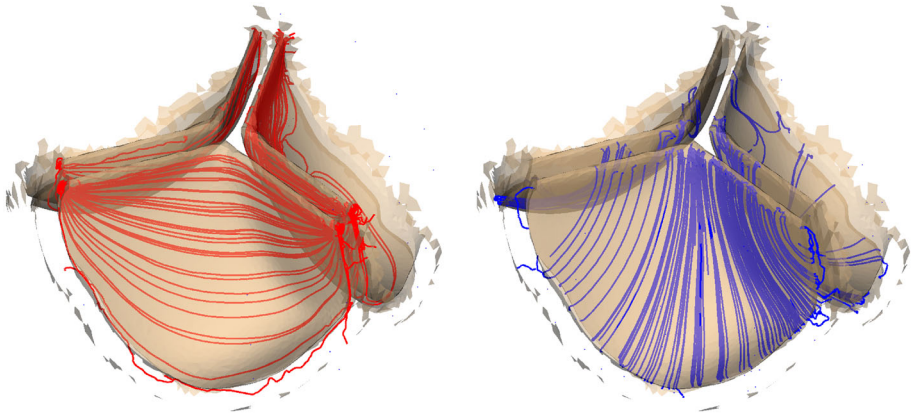

FIGURE 4. A visualization of the circumferential (left) and radial (right) vector fields defined on the valve mesh. The valve material model depends on these fields in order to describe mechanical anisotropy.

Construction of the Valve Assembly Model

Cylindrical extensions are appended to the inlet and outlet of the processed aortic surface model. A closed boundary representation of the volumetric aorta is generated within Meshmixer as an extrusion by a constant amount of 1.2 mm. This value approximates the average aortic thickness in the region of interest.[32]

The volumetric models of the valve and the aorta are smoothly combined in Meshmixer to obtain a closed boundary representation of the combined aorta and valve geometry. TetWild[3] is used to generate a tetrahedral finite element mesh of the combined valve and aorta volumetric model. The tetrahedral mesh element edge lengths vary approximately between 0.3 mm (near the lumen and valve leaflets) and 0.6 mm (near the outer surface).

Various sets of edges, faces and elements in the tetrahedral mesh are labeled to identify regions of the model with different material properties and for applying boundary conditions. For example, edges on the ends of the cylindrical extensions are labeled to identify the inlet and outlet of flow.

Simulation of Flow Through the Constructed Valve Model

The generated valve geometries are simulated using an approach called the immersed boundary method, which was created by Peskin for simulating heart valve leaflets interacting with blood.[24,25] The version of the immersed boundary method used herein, called the immersed finite element/difference method, treats the aortic wall and valve leaflets as hyperelastic materials. The leaflets are assumed to be mechanically anisotropic. Their stresses depend on several vector fields which are depicted in Fig. 4. The *circumferential* vector field is in the left panel and also shown in the paper by Hasan *et al.*[12] The *radial* vector field is in the right panel. For more details on the immersed finite element/difference method, the numerical discretization used in this paper, and the setup for the material models, refer to Griffith and Luo and Boffi *et al.*,[5,10] the Immersed Boundary Adaptive Mesh Refinement (IBAMR) webpage,[8] and the Supplementary Material.

Cardiac catheterization data are also available for the selected patient. These data include pressure time-series in various parts of the circulation from which physiologic boundary conditions for the FSI simulations are derived. Pointwise pressure boundary conditions are imposed on the combined aorta and aortic valve model in locations upstream from the valve and downstream at the bend in the aortic arch. The pressure boundary condition upstream from the valve is a synthetically derived left ventricular pressure waveform, and the downstream pressure boundary condition is calculated from a three-element windkessel model.

RESULTS

The results consist of patient-specific valve geometries constructed for several subjects along with FSI simulations using a valve geometry from a selected patient. The method described here is applied to 25 pediatric patients. Figure 5 depicts images of the volumetric valve models created for these patients.

Figures 6 and 7 show results from a spatially adaptive FSI simulation using the valve assembly model. The columns indicate different snapshots in time over the course of a cardiac cycle. The Cartesian

[3]https://github.com/Yixin-Hu/TetWild, an open-source tool for generating meshes of complex geometries.[13]

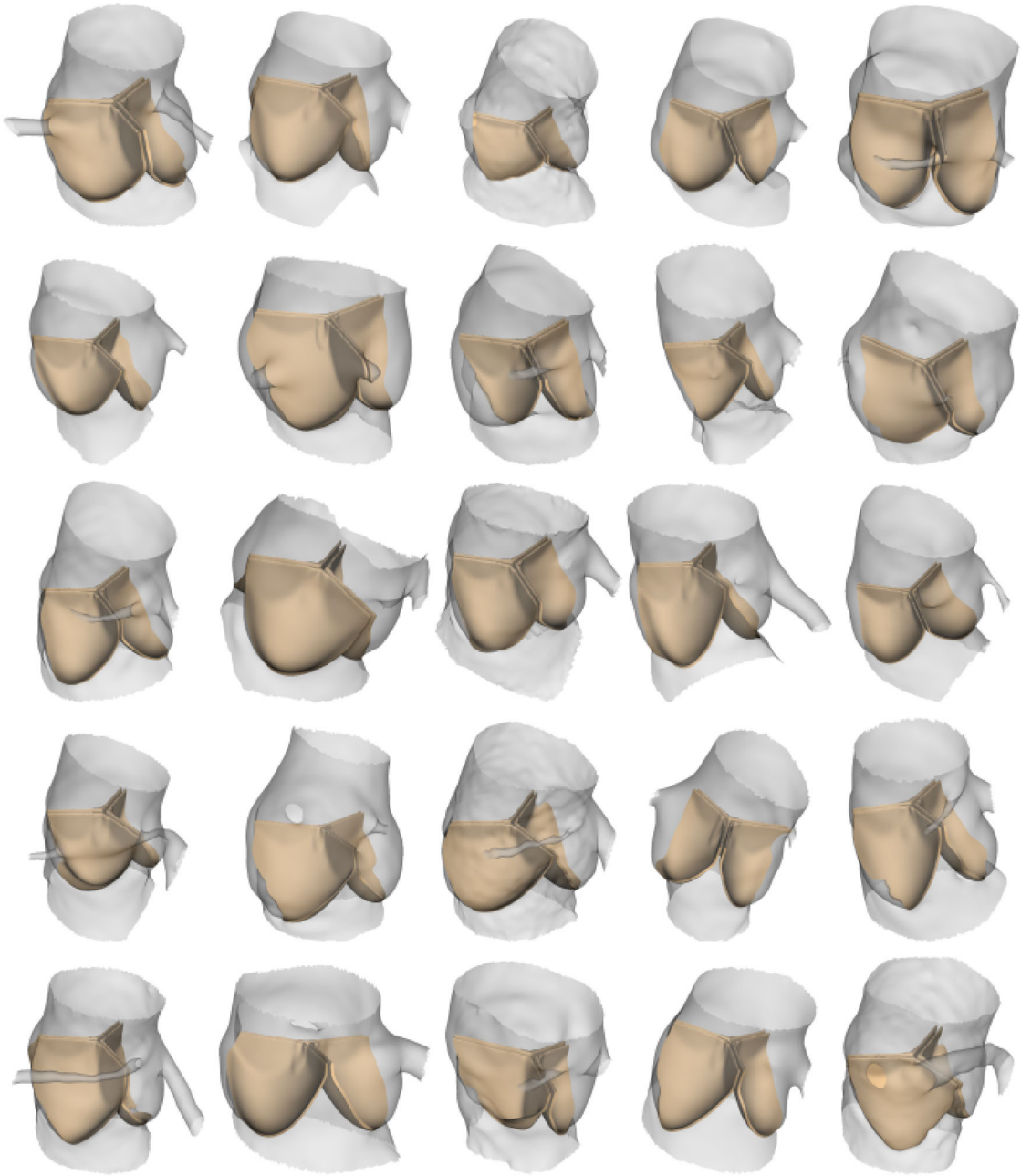

FIGURE 5. Patient-specific valve anatomical models for each of the 25 pediatric patients visualized within a segmentation of the aortic root and sinuses.

cell size on the finest level is 0.32 mm for this simulation.

Figure 8 depicts the pressure and flow waveforms over approximately three cardiac cycles. Flow waveforms are calculated as the flux of the velocity field through the boundary surfaces of the computational domain that intersect the aortic lumen. The pressure waveforms shown are the applied boundary conditions, with the aortic pressure updated from a windkessel model using the flow (calculated as the flux of the velocity field downstream from the valve) measured at the boundary of the computational domain. Only the flow waveform calculated upstream from the valve is shown. The ventricular pressure waveform, shown in grey, is the pressure on the boundary upstream of the valve. The aortic pressure waveform, shown in black, is the pressure on the boundary downstream of the valve. A study of mesh refinement and convergence to a periodic steady state is included in the Supplementary Material.

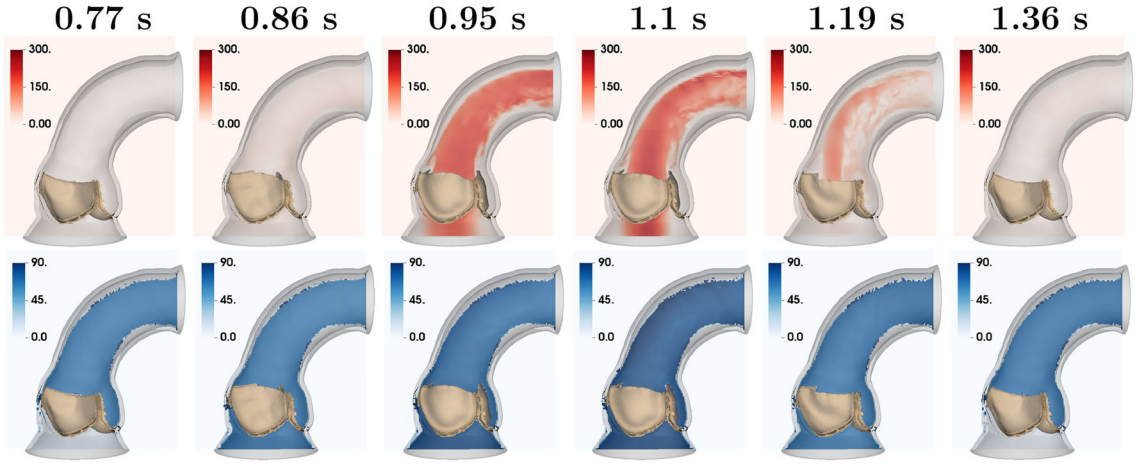

FIGURE 6. The top row shows snapshots, over a complete cardiac cycle, of the magnitude of the fluid velocity field in cm/s on a slice of the computational domain that bisects the ascending aorta. The bottom row shows the blood pressure in mmHg on the same slice. Both sequences of panels also show deformations of the aortic valve and aorta.

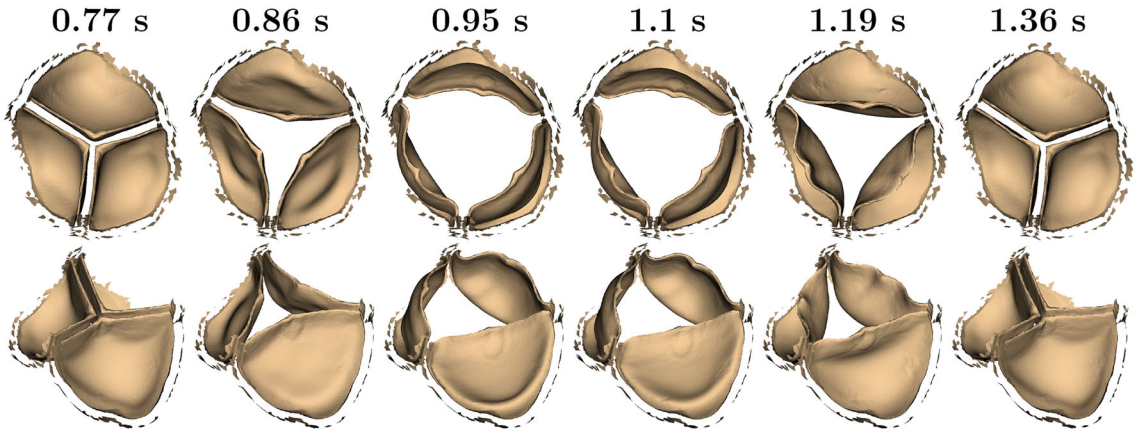

FIGURE 7. Selected snapshots of the valve over the course of a cardiac cycle.

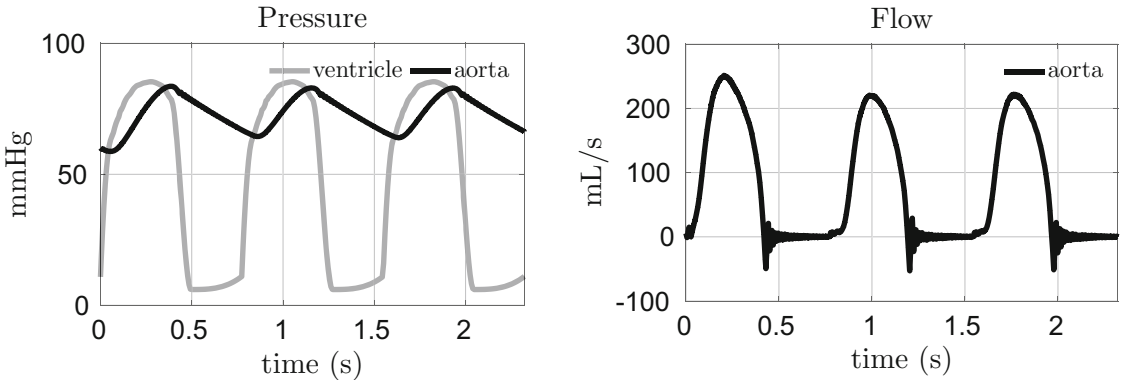

FIGURE 8. Pressure and flow waveforms from the simulation.

DISCUSSION

Patient-specific FSI simulations of the aortic valve and aorta require geometries for the leaflets and aortic wall. Whereas clinically acquired CTA images can be used to render the geometry of the aortic lumen, the resolution is usually too coarse for reconstructing a sufficiently accurate geometry of the valve leaflets. Computer models that include the aortic valve typically use an idealized geometry that is manually reg-

istered with the vessel lumen using computer-aided-design software.[12] This process is often tedious and involves manual scaling, translation, and rotation of the idealized leaflets. Further, this procedure does not take into account possible asymmetry in the aortic sinuses and corresponding leaflets.

The process for selecting sinus data samples from the CTA segmentation and generating the volumetric valve geometries, shown in Fig. 5, currently takes less than 30 minutes per valve. The lower leaflet surfaces, which contain the essential geometric information, are constructed in a matter of minutes. The alternative approach requires manual registration of idealized valve geometries. This can take several hours depending on the transformations required. However, the main concern is the subjectivity introduced in manually transforming and scaling idealized leaflets to fit a patient's aortic geometry. If sinus samples can be reliably and consistently identified from the CTA segmentation, the semi-automated approach described in this paper does not suffer from this issue.

Figure 5 demonstrates the applicability of this procedure on a modest number of pediatric patients. These patients have normal aortic anatomy but abnormal coronary artery anatomy. A future study will involve FSI simulation of blood flow in models for both the aorta and coronary arteries of this patient population. Given the important interactions between coronary flow and the valve leaflets,[6] a systematic approach to construct patient-specific leaflet geometries for a cohort of subjects will be necessary. Models generated using this approach could be modified to study calcified aortic leaflets or bicuspid valve disease. The former would require changes to the thickness profile and/or the material models, and the latter would require fusing two leaflets. These modifications can be implemented independently from the geometric construction procedure of the leaflets.

Several existing methods for constructing aortic valve geometries rely, in some form, on the identification of the *interleaflet triangles*,[31] i.e., the leaflets' basal edges. These physiologic landmarks are used either as a boundary condition for the equations of mechanical equilibrium[16] or as a set of control points for mapping to patient-specific geometries.[22] The procedure presented in this paper is most similar to the method presented by Morganti *et al.*[22] Those authors used CT data along with the interleaflet triangle curves to build NURBS surfaces of the leaflets. In contrast to the approach in this paper, their leaflets were constructed in the open configuration and were assumed to have uniform thickness. The leaflet construction presented here, done in the closed configuration, allows for the imposition of a parabolic leaflet shape[21] as well as the inclusion of the valve center in the geometry, provided that this point can be identified in the CTA data. Liang *et al.* implemented a machine learning procedure using CT data.[19] Their leaflet geometries were computed in the closed configuration and relied on landmarks from sinus samples. However, their training set required direct segmentations of valve geometries from imaging data, which is generally not possible with CTA images, as used in this study. Furthermore, machine learning approaches lack interpretability. An advantage of the approach presented here is the concrete formulation used to fit valve leaflet geometries to data in the form of a constrained optimization problem.

Figures 6, 7, and 8 demonstrate that a valve geometry, when created for one patient and placed in the valve assembly model, operates in a reasonable manner under physiologic driving and loading conditions. The valve opens when the ventricular pressure exceeds the downstream pressure. There is a difference between the ventricular and aortic pressures when the valve is open. This pressure gradient also appears in clinical data (see, for example, the waveforms in Murgo *et al.*[23] and related simulation results in Hasan *et al.*[12]). Figure 7 focuses on the leaflet dynamics over the course of a single cardiac cycle. The leaflets open and close as expected. Sealing of the leaflets during diastole is confirmed by the flow waveforms shown in Fig. 8. In general, the shapes of the pressure and flow waveforms compare well with those measured clinically.[23]

The procedure and study presented in this paper have several limitations. As shown in the recent work of Rego *et al.*,[27] leaflet thickness is heterogenous and certainly deviates from the imposition of a single symmetric thickness profile. Furthermore, the selection of sinus samples, corresponding to the interleaflet triangles, is a manual part of the process presented in this study. Small changes to the sinus samples can have a substantial effect on the generated leaflet geometries. In future versions of this method, robustness of the sinus sample selection can be improved by choosing thicker strips to represent the samples. These thicker samples will be less sensitive to outliers. The weighting strategies should help emphasize particular parts of the samples to the optimizer that are closer to the target anatomical features, thus limiting potential loss of accuracy despite reduced precision of the samples. Lastly, this procedure has not been validated with the appropriate clinical data. Such data might include clinical images from which *in vivo* leaflet geometries can be derived and/or fluid mechanical data (such as 4D-flow images) that can be compared to results from FSI simulations of the valve assembly model. Validation will be the focus of future work.

SUPPLEMENTARY INFORMATION

The online version of this article contains supplementary material available https://doi.org/10.1007/s10439-022-03075-z.

ACKNOWLEDGMENTS

The authors thank Kristina Montez for many helpful suggestions.

CONFLICT OF INTEREST

No conflicts of interest are declared.

FUNDING

This study was supported by National Science Foundation (Grant Nos. OAC 1652541 and OAC 1931516) and National Institutes of Health (Grant Nos. R01HL157631 and U01HL143336).

REFERENCES

[1]Assey, M. E., M. R. Zile, B. W. Usher, M. P. Karavan, and B. A. Carabello. Effect of catheter positioning on the variability of measured gradient in aortic stenosis. *Cathet. Cardiovasc. Diagn.* 30:287–292, 1993.

[2]Bellhouse, B. Velocity and pressure distributions in the aortic valve. *J. Fluid Mech.* 37:587–600, 1969.

[3]Bellhouse, B., and F. Bellhouse. Mechanism of closure of the aortic valve. *Nature* 217:86–87, 1968.

[4]Bellhouse, B., and L. Talbot. The fluid mechanics of the aortic valve. *J. Fluid Mech.* 35:721–735, 1969.

[5]Boffi, D., L. Gastaldi, L. Heltai, and C. S. Peskin. On the hyper-elastic formulation of the immersed boundary method. *Comput. Methods Appl. Mech. Eng.* 197:2210–2231, 2008.

[6]Cao, K., and P. Sucosky. Aortic valve leaflet wall shear stress characterization revisited: impact of coronary flow. *Computer Methods Biomech. Biomed. Eng.* 20:468–470, 2017.

[7]Chen, H., B. Yeats, K. Swamy, M. Samaee, S. K. Sivakumar, F. Esmailie, A. Razavi, P. Yadav, V. H. Thourani, V. Polsani *et al.* Image registration-based method for reconstructing transcatheter heart valve geometry from patient-specific CT scans. *Ann. Biomed. Eng.* 50(7):805–815, 2022.

[8]Griffith, B. E. IBAMR: an adaptive and distributed-memory parallel implementation of the immersed boundary method. https://github.com/IBAMR/IBAMR.

[9]Griffith, B. E. Immersed boundary model of aortic heart valve dynamics with physiological driving and loading conditions. *Int. J. Numer. Methods Biomed. Eng.* 28:317–345, 2012.

[10]Griffith, B. E., and X. Luo. Hybrid finite difference/finite element immersed boundary method. *Int. J. Numer. Methods Biomed. Eng.* 33:e2888, 2017.

[11]Haj-Ali, R., G. Marom, S. B. Zekry, M. Rosenfeld, and E. Raanani. A general three-dimensional parametric geometry of the native aortic valve and root for biomechanical modeling. *J. Biomech.* 45:2392–2397, 2012.

[12]Hasan, A., E. M. Kolahdouz, A. Enquobahrie, T. G. Caranasos, J. P. Vavalle, and B. E. Griffith. Image-based immersed boundary model of the aortic root. *Med. Eng. Phys.* 47:72–84, 2017.

[13]Hu, Y., Q. Zhou, X. Gao, A. Jacobson, D. Zorin, and D. Panozzo. Tetrahedral meshing in the wild. *ACM Trans. Graph.* 37:60:1–60:14, 2018.

[14]Johnson, E. L., D. W. Laurence, F. Xu, C. E. Crisp, A. Mir, H. M. Burkhart, C.-H. Lee, and M.-C. Hsu. Parameterization, geometric modeling, and isogeometric analysis of tricuspid valves. *Comput. Methods Appl. Mech. Eng.* 384:113960, 2021.

[15]Kaiser, A. D., D. M. McQueen, and C. S. Peskin. Modeling the mitral valve. *Int. J. Numer. Methods Biomed. Eng.* 35:e3240, 2019.

[16]Kaiser, A. D., R. Shad, W. Hiesinger, and A. L. Marsden. A design-based model of the aortic valve for fluid–structure interaction. *Biomech. Model. Mechanobiol.* 20:2413–2435, 2021.

[17]Khalighi, A. H., A. Drach, R. C. Gorman, J. H. Gorman, and M. S. Sacks. Multi-resolution geometric modeling of the mitral heart valve leaflets. *Biomech. Model. Mechanobiol.* 17:351–366, 2018.

[18]Lee, J. H., A. D. Rygg, E. M. Kolahdouz, S. Rossi, S. M. Retta, N. Duraiswamy, L. N. Scotten, B. A. Craven, and B. E. Griffith. Fluid-structure interaction models of bioprosthetic heart valve dynamics in an experimental pulse duplicator. *Ann. Biomed. Eng.* 48:1475–1490, 2020.

[19]Liang, L., F. Kong, C. Martin, T. Pham, Q. Wang, J. Duncan, and W. Sun. Machine learning-based 3-D geometry reconstruction and modeling of aortic valve deformation using 3-D computed tomography images. *Int. J. Numer. Methods Biomed. Eng.* 33:e2827, 2017.

[20]Mathur, M., W. D. Meador, M. Malinowski, T. Jazwiec, T. A. Timek, and M. K. Rausch. Texas trivalve 1.0: a reverse-engineered, open model of the human tricuspid valve. *Eng. Comput.*, 2022. https://doi.org/10.1007/s00366-022-01659-w.

[21]Mercer, J., M. Benedicty, and H. Bahnson. The geometry and construction of the aortic leaflet. *J. Thorac. Cardiovasc. Surg.* 65:511–518, 1973.

[22]Morganti, S., F. Auricchio, D. Benson, F. Gambarin, S. Hartmann, T. Hughes, and A. Reali. Patient-specific isogeometric structural analysis of aortic valve closure. *Comput. Methods Appl. Mech. Eng.* 284:508–520, 2015.

[23]Murgo, J. P., N. Westerhof, J. P. Giolma, and S. A. Altobelli. Aortic input impedance in normal man: relationship to pressure wave forms. *Circulation* 62:105–116, 1980.

[24]Peskin, C. S. Flow patterns around heart valves: a numerical method. *J. Comput. Phys.* 10:252–271, 1972.

[25]Peskin, C. S. Numerical analysis of blood flow in the heart. *J. Comput. Phys.* 25:220–252, 1977.

[26]Peskin, C. S. and D. M. McQueen. Mechanical equilibrium determines the fractal fiber architecture of aortic heart valve leaflets. *Am. J. Physiol. Heart Circ. Physiol.* 266:H319–H328, 1994.

[27]Rego, B. V., A. M. Pouch, J. H. Gorman, R. C. Gorman, and M. S. Sacks. Patient-specific quantification of normal and bicuspid aortic valve leaflet deformations from clinically derived images. *Ann. Biomed. Eng*. 50(1):1–15, 2022.
[28]Sahasakul, Y., W. D. Edwards, J. M. Naessens, and A. J. Tajik. Age-related changes in aortic and mitral valve thickness: implications for two-dimensional echocardiography based on an autopsy study of 200 normal human hearts. *Am. J. Cardiol*. 62:424–430, 1988.
[29]Siu, S. C., and C. K. Silversides. Bicuspid aortic valve disease. *J. Am. Coll. Cardiol*. 55:2789–2800, 2010.
[30]Stein, P. D. and H. N. Sabbah. Turbulent blood flow in the ascending aorta of humans with normal and diseased aortic valves. *Circ. Res*. 39:58–65, 1976.
[31]Sutton III, J. P., S. Y. Ho, and R. H. Anderson. The forgotten interleaflet triangles: a review of the surgical anatomy of the aortic valve. *Ann. Thorac. Surg*. 59:419–427, 1995.
[32]Tran, A., B. Burkhardt, A. Tandon, S. Blumenschein, A. van Engelen, M. Cecelja, S. Zhang, S. Uribe, J. Mura, G. Greil et al. Pediatric heterozygous familial hypercholesterolemia patients have locally increased aortic pulse wave velocity and wall thickness at the aortic root. *Int. J. Cardiovasc. Imaging* 35:1903–1911, 2019.